Research Article Vol. 9, No. 1 | 1 Jan 2019 | OPTICAL MATERIALS EXPRESS 269

Optical Materials EXPRESS

Temperature calculation in metal substrates during two-photon polymerization

EMELY MARIE HARNISCH,[1,*] TOMMY VENEK,[1] SVENJA NOHR,[1] NIELS KÖNIG,[1] AND ROBERT SCHMITT[1,2]

[1] *Department of Production Metrology, Fraunhofer Institute for Production Technology IPT, Aachen, 52074, Germany*
[2] *Laboratory for Machine Tools and Production Engineering WZL, RWTH Aachen University, Aachen, 52074, Germany*
[*] *emely.harnisch@ipt.fraunhofer.de*

Abstract: The two temperature model (TTM) as well as the heat conduction equation (HCE) are used to calculate the temperature at surfaces of metal substrates during two-photon polymerization (TPP). Using TTM, the change in reflectivity of the material during one laser pulse is simulated for different initial temperatures. In addition, experiments with tempered metal substrates are performed to examine how the change of the material properties due to different temperatures influence the polymerization process.

1. Introduction

Since two-photon polymerization (TPP) was first introduced in the 1990ies [1], it has become an established structuring technology in science. A lot of research groups all over the world are using the technique for fabricating e.g. microoptical elements, biological structures, photonic crystals or bionic surfaces [2–4]. The establishment of this technology goes hand in hand with the growing demand for individual microstructures of the photonic market [5] and in cell biology [6].

Due to its high number of degrees of freedom, providing full 3D capability while allowing for feature sizes beyond the diffraction limit [7], it is of high interest to establish TPP as a mastering technique for production. To gain a high throughput, it has to be embedded into a process chain for molding [8], causing the usable number of dimensions to be limited to 2.5. Nevertheless, in comparison to traditional structuring methods like cutting and lithographic ones, the technology offers advantages regarding complexity of geometries and thus design freedom.

A proven molding technique for high throughput production of optical elements is injection molding. Since this process is known for its harsh conditions like high pressures and temperatures, stable substrates like metal ones have to be used. Writing directly on metal surfaces with TPP is very interesting, because also curved molding tools can be equipped with individual micro- or nanostructures. Preliminary experiments showed, that TPP on metal surfaces implies challenges like back reflections, that lead to stationary waves, strong blistering and a reduced dynamic range of usable laser power [9], see also Fig. 1.

Comprehensive work regarding TPP on metal and opaque surfaces was already performed by Rekstyte et al. within the context of structuring implants for an improved cell attachment. The researcher examined silicon as well as different metals like chrome, titanium, gold, aluminium and iron, partly with different roughnesses. Results showed, that the increase of line width and height depends on the material and its reflectivity. Rekstyte et al. were able to fabricate up to threedimensional structures on the substrates without quality loss due to roughness and reflectivity [10–12]. Similar experiments on black silicon were shown by Zukauskas et al. [13]. The effect of the stationary wave due to back reflections during TPP on gold surfaces was comprehensively discussed by Rheinhardt et al. [14]. In [15], Stankevicius et al. examined how the pulse duration and repetition rate of the laser affects the polymerization process

#348088 https://doi.org/10.1364/OME.9.000269
Journal © 2019 Received 12 Oct 2018; revised 19 Nov 2018; accepted 19 Nov 2018; published 20 Dec 2018

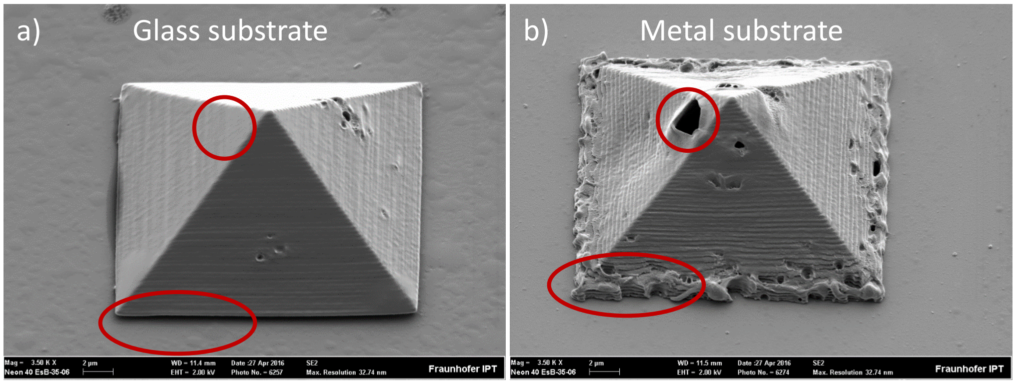

Fig. 1. (a) Pyramid written with TPP on a glass substrate, (b) Pyramid written with TPP on a metal substrate. Each pyramid has a height of 10 μm, an edge length of 20 μm and was written with 16 mW and 1000 $\mu m/s$ in IP-Dip.

during interference lithography. Due to their experiments and calculations concerning substrate temperature and the dynamics of the radicals in the polymer, they found out, that changes in the radical concentration, thermal accumulation and the diffusion of oxygen from the surrounding strongly influence the shape of polymerized areas.

When regarding TPP on metal surfaces, three areas have to be considered: The heating of the substrate due to absorption of laser power, the shape of a stationary wave occuring due to the superposition of incoming and reflected light and the polymerization process, that is influenced by the temperature on the metal substrate and the intensity distribution of the stationary wave. In the context of pulsed laser light interacting with metal surfaces, it must be distinguished between the two temperature model, that describes the electron and ion temperature as well as changes in reflectivity and the complex refractive index and the heat conduction equation. The HCE calculates the metal temperature in dependence on material properties like the heat conduction or heat capacity in a more macroscopic manner.

For a better control of TPP on metal surfaces, a model for describing the heating of metal substrates during TPP is presented within this paper. The heat conduction equation (HCE) as well as the two temperature model (TTM) are used to calculate the temperature in the metal. In addition, experiments with tempered metal substrates are performed to examine the influence of the substrate temperature on the polymerization process.

2. Calculation of the temperature with the heat conduction equation

In TPP, a pulsed laser is focused through liquid photosensitive polymer on the surface of a glass or metal substrate. For the latter, dip-in lithography is a possible method, where the substrate and photopolymer is used in an upside-down arrangement [16]. Due to the spatial and temporal concentration of energy, the polymer is exposed within a volumetric pixel, called voxel, in the focus. By moving the laser in lateral direction through the polymer and the substrate in axial direction, arbitrary geometries can be fabricated. To simplify the calculation of the temperature, only the writing of single lines in x-direction is regarded. The following thermic energy equation describes the temperature field in a metal substrate caused by a focused laser [17]:

$$\rho \cdot c_p \left[\frac{\partial T}{\partial t} + \vec{v} \cdot \vec{\nabla} T \right] = \lambda \cdot \vec{\nabla}^2 T + Q_L(x, y, z) \tag{1}$$

Where ρ is the density of the metal, c_p is the specific heat capacity, T the temperature, $\vec{v}$ the velocity, λ the thermal conductivity and Q_L corresponds to a heat source with the unit power

(Watt) per volume (cubic meter). The first term of Eq. 1 represents the change of temperature with time. Convection is given by the second term and accords to the motion of the substrate, respectively the laser in this case. Diffusion and heat input from the laser are described by the two terms on the right side, while the time average of the laser power is used.

2.1. Discretization of the HCE

For a numerical solution of the HCE via a linear system of equations, it has to be discretized with the finite volume method (FVM). To do so, the regarded simulation area is divided into reference units in a Cartesian coordinate system. Fig. 2 illustrates the arrangement of the control volumes as a right-handed coordinate system [18]: While the x-axis represents the west-east direction and the y-axis accordingly the south-north direction, the z-axis is assigned to a down-up link. Starting from the center point C in the middle of the regarded reference unit P, the spatial steps δx_w, δx_e, δx_s, δx_n, δx_d and δx_u represent the distances to the centers of the adjacent reference units in the corresponding directions. The edge lengths Δx, Δy and Δz define the size of a control volume [18]. In a first step, Eq. 1 has to be integrated over a reference cell, resulting in Eq. 2

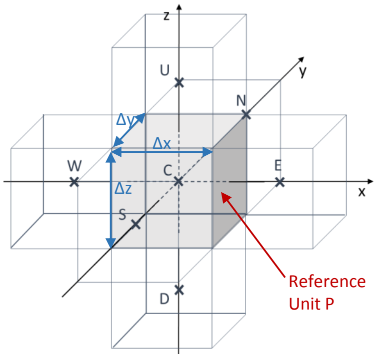

Fig. 2. Arrangement of control units for the discretization of the HCE.

$$\int\limits_{t}^{t+\Delta t}\int\limits_{d}^{u}\int\limits_{s}^{n}\int\limits_{w}^{e} \rho c_p \frac{\partial T}{\partial t} dxdydzdt + \int\limits_{t}^{t+\Delta t}\int\limits_{d}^{u}\int\limits_{s}^{n}\int\limits_{w}^{e} \rho c_p \vec{v}\cdot\vec{\nabla}T\,dxdydzdt$$
$$= \int\limits_{t}^{t+\Delta t}\int\limits_{d}^{u}\int\limits_{s}^{n}\int\limits_{w}^{o} \left(\lambda \cdot \vec{\nabla}^2 T + Q_L(x,y,z)\right) dxdydzdt. \tag{2}$$

To consider the change of temperature T within $t + \Delta t$, following expression is used for the time independent part:

$$\int\limits_{t}^{t+\Delta t} T\,dt = \Delta t \cdot T_p^{n+1} \tag{3}$$

For a better clarity, the following expressions are used to outline the discretized HCE [19], where $P_{e,i}$is the Peclet number P_e and the index i is used to show which unit is regarded. Since the Peclet number corresponds to the ratio of convection to diffusion and convection is only regarded in x-direction, the index i can become w or e.

$$F = \rho c_p \vec{v} \Delta x_i \Delta y_i \qquad P_{e,i} = \frac{\rho c_p \vec{v} \frac{\partial T}{\partial x}}{\frac{\partial T}{\partial x}\left(\lambda \frac{\partial T}{\partial x}\right)} \qquad A(P_{e,i}) = 1 - \left|\frac{P_{e,i}}{2}\right| \tag{4}$$

(5)

The discretised HCE follows as

$$\begin{aligned} \frac{\rho c_p \Delta x \Delta y \Delta z}{\Delta t} \cdot T_p^n + \bar{Q} \Delta x \Delta y \Delta z = [\ \lambda_n \frac{\Delta x \Delta z}{\delta y_n} - \lambda_s \frac{\Delta x \Delta z}{\delta y_s} + \left[\lambda_e \frac{\Delta x \Delta y}{\delta x_e A\left(P_{e,e}\right)} + max\left(0, -F\right)\right] \\ - \left[\lambda_w \frac{\Delta x \Delta y}{\delta x_w A\left(P_{e,w}\right)} + max\left(0, -F\right)\right] + \lambda_u \frac{\Delta x \Delta y}{\delta z_u} - \lambda_d \frac{\Delta x \Delta y}{\delta z_d}\ ] \cdot T_p^{n+1} \\ -\lambda_n \frac{\Delta x \Delta z}{\delta y_n} \cdot T_n^{n+1} + \lambda_s \frac{\Delta x \Delta z}{\delta y_s} \cdot T_s^{n+1} - \left[\lambda_e \frac{\Delta x \Delta y}{\delta x_e A\left(P_{e,e}\right)} + max\left(0, -F\right)\right] \cdot T_e^{n+1} \\ + \left[\lambda_w \frac{\Delta x \Delta y}{\delta x_w A\left(P_{e,w}\right)} + max\left(0, -F\right)\right] \cdot T_w^{n+1} - \lambda_u \frac{\Delta x \Delta y}{\delta z_u} \cdot T_u^{n+1} - \lambda_d \frac{\Delta x \Delta y}{\delta z_d} \cdot T_d^{n+1}, \end{aligned} \tag{6}$$

where the volumetric source term is described by the laser power per cubic meter

$$Q_L(x, y, z) = I_0(1 - R)\frac{\Delta A}{\Delta V} \cdot \left[e^{-\alpha z} - e^{-\alpha(z+\Delta z)}\right] \cdot e^{-2\left(\frac{x^2+y^2}{r_L^2}\right)}. \tag{7}$$

With $I_0 = \frac{2\bar{P}_L}{\pi r_L^2} T_{obj}$, where $\bar{P}_L$ is the time average of the laser power, r_L represents the radius of the laser focus, α the attenuation index and T_{obj} corresponds to the transmission of the microscope objective. In Eq. 7, R is the reflectivity of the regarded surface and the middle term $\frac{\Delta A}{\Delta V} \cdot \left[e^{-\alpha z} - e^{-\alpha(z+\Delta z)}\right]$ considers the attenuation of the laser intensity along the height of a unit cell Δz with volume ΔV as well as upper and bottom surface ΔA perpendicular to the z-direction. The index P in T_p^n signals, that reference unit P is regarded at time step n, respectively in T_p^{n+1} at time step $n + 1$.

2.2. Simulation of the temperature during TPP

Since the background of this simulation is to control TPP on metal surfaces for structuring molding tools, corresponding materials were chosen for the temperature calculation. Three established metals for the fabrication of molding tools are steel 1.2083 [20], brass CuZn37 [21] and aluminium RSA 905 [22], while the according parameters are given in table 1. The absorption coefficient for steel was calculated with the formula $\alpha = \frac{4 \cdot \pi \cdot k}{\lambda}$ from [23] (with k being the amount of the imaginary part of the complex refractive index), while the complex refractive index was derived from [24] for stainless steel, since no data for steel 1.2083 was found.

Evaluation was performed by measuring the highest temperature in the middle of the Gaussian temperature distribution. The results in Fig. 3 show, that the temperature increases linearly with the laser power from 10 mW to 50 mW and nearly no influence is given by the variation of the laser scanning speed between 100 $\mu m/s$ and 1000 $\mu m/s$. Due to its high heat conduction and reflectivity, the lowest temperatures are reached on brass, since a smaller amount of energy is coupled into the material and the heat quickly dissipates. Due to the same reasons, a small heat conduction and reflectivity, the highest temperatures are found in steel. Initial temperature for the calculation was 298 K. For aluminium and brass, no influence of the writing speed on the resulting temperature was observed. Thus, only regarding the temperature in the substrate, brass seems to be most appropriate for structuring with TPP, since it heats up least.

Table 1. Material properties of the metals used for the simulation.

Material	Steel 1.2083	Aluminium RSA 905	Brass CuZn37
Heat capacity c_p $[\frac{J}{kg \cdot K}]$	460 [25]	897 [26]	377 [28]
Heat conduction λ $[\frac{W}{m \cdot K}]$	16 [25]	115 [27]	120 [28]
Density ρ $[\frac{kg}{m^3}]$	7800 [25]	2950 [27]	8440 [28]
Extinction coefficient α $[\frac{1}{m}]$	$8.25 \cdot 10^7$	$13.51 \cdot 10^7$ [29]	$7.63 \cdot 10^7$ [30]
Reflectivity R (measured)	0.6	0.74	0.92

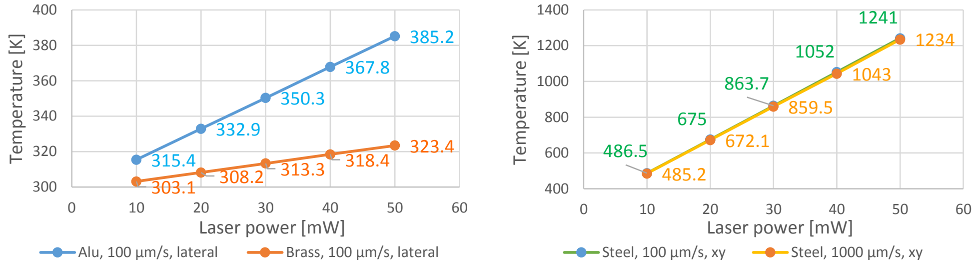

Fig. 3. Resulting maximum temperatures for (a) aluminium and brass and (b) steel, each for varying laser powers at 100 $\mu m/s$ and for steel also at 1000$\mu m/s$.

All calculations were performed with a laser wavelength of 780 nm, a pulse duration of 100 fs and a repetition rate of 80 MHz. A special metal thickness was not considered within the simulation, since the platelets used in the experiment have a thickness of 6 mm, that is comparable to infinity when considering the voxel size of 360 nm and the penetration depth. Scanning speeds of 100 $\mu m/s$ and 1000 $\mu m/s$ were chosen due to the aim of a high throughput during structure fabrication.

For steel, also calculations with a varying initial temperature were performed at 50 mW and a scanning speed of 100 $\mu m/s$. Corresponding to the experiments in chapter 4, the temperature was varied from 5°C to 80°C (283K and 358 K). Results show, that the final temperature increase linearly in dependence on the initial temperature, and that the change in the initial temperature is simply added to the results shown in Fig. 3 for 50 mW and 100 $\mu m/s$, see Fig. 4.

3. Calculation of the temperature with the two temperature model

Regarding material processing with laser pulses in the femtosecond range, there is a thermic non-equilibrium between the electrons and the ions. Consequently, the whole system is described by the two coupled differential equations 8 and 9, one for the electrons and one for the ions. Due to scattering processes, an equilibrium between the two systems can be established. If the time between two scattering processes is in the order of the duration of one laser pulse, the TTM has to be applied [31].

$$\frac{\partial U_e(t,z)}{\partial t} = \frac{\partial C_e(T_e)T_e(t,z))}{\partial t} = \frac{\partial}{\partial z}(\dot{q}_e) - G(T_e,T_i)(T_e - T_i) + Q(t,z) \tag{8}$$

$$\frac{\partial U_i(t,z)}{\partial t} = \frac{\partial C_i(T_i)T_i(t,z))}{\partial t} = G(T_e,T_i)(T_e - T_i) \tag{9}$$

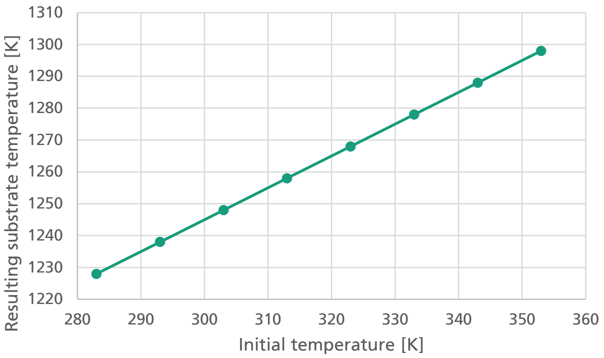

Fig. 4. Resulting temperatures in steel for 50 mW, 100 $\mu m/s$ and varying initial temperatures from 10°C to 80°C.

$C_e(T_e)$ is the heat capacity of the electrons, $C_i(T_i)$ the one for the ions and $G(T_e, T_i)$ corresponds to the coupling factor due to scattering. The first terms of both equations represent the change of the internal energy U, caused by diffusion flows, heat exchanges between electron and ions and the absorbed laser power. q is the heat flow due to heat conductivity and Q the absorbed laser power, which is only considered in the equation for the electrons. To take into account a delay of the heat conduction, the heat conduction model according to Cattaneo was used [32]. The temperature dependence of the heat capacity of the electrons is derived from literature and given by equation 10. Here, u_e is the internal energy of the electrons referred to the volume and is defined by the Fermi distribution f_F, the density of the energy levels g_e and the corresponding energy level E. An overview of the Fermi temperatures, energies and electron densities for calculating C_e is given in [33] for a choice of metals. Heat conduction of the electrons and its temperature dependences are determined, based on Drude's model.

$$C_e(T_e) = \frac{\partial u_e}{\partial T_e} = \int_0^\infty \frac{\partial f_F(E, \mu, T_e)}{\partial T_e} g_e(E) E dE \tag{10}$$

Since the heat capacity of the ions mainly determines the heat capacity of the metal, it will be regarded in the following. Based on the phonon formalism and using the Debye model, Eq. 11 is given for the heat capacity of the ions, where the left one is the general form and the right one corresponds to a limit value observation for high temperatures, causing $C_i(T_i)$ to become constant [34]. In case of high temperatures (e.g. the Debye temperature), the approach of Dulong-Petit has to be used: $C_i(T_i) = 3n_i k_B$ with the density of energy levels n_i. This expression will be used in this model.

$$C_i(T_i) = 9\frac{N_i}{V} k_B \left(\frac{T_l}{T_D}\right)^3 \int_0^{\frac{T_D}{T_l}} \frac{\vartheta e^\vartheta}{\left(e^\vartheta - 1\right)^2} d\vartheta \qquad C_i(T_i) = 3n_i k_B \tag{11}$$

with the ion density N_i/V, the Debye temperature T_D, the absolute temperature T_l and the Boltzmann constant k_B. ϑ is given by the expression $\vartheta = h\omega_D/k_B T_i$, where h is the Planck constant and ω_D the Debye frequency. Consequently, the heat capacity of the ions corresponds to the derivation of the internal energy of the phonons with respect to the temperature [35]. In comparison to the heat conduction of the electrons, the heat conduction of the ions is very small and can be neglected.

The maximum temperature is also influenced by the electron-ion coupling factor and its dependence on the temperature [36]. Due to the proportional dependence on the electron- as well as on the ion temperature, the coupling factor increases during absorption of laser power, causing a higher heat flow from the electron to the ion system. Thus, the increase of the electron temperature is damped and that of the ions is accelerated, resulting in the following Eq. 12.

$$G(T_e, T_i) = \frac{\pi^2 m_e v_l^2 n_e}{6\tau_e(T_e, T_i)T_e} \qquad G(T_e = T_i = T_{room}) = \frac{\pi^2 m_e v_l^2 n_e}{6B} = const. \tag{12}$$

This expression becomes constant for $T_e = T_i$ =room temperature, m_e is the mass of an electron.

To describe the source term of the laser Q(x,t) with the absorption coefficient α, the pulse duration t_P, J_L the exposure dose and R the substrate's reflectivity is given [37]. The reflectivity R is calculated from the complex refractive index, which is derived from the complex dielectric conduction.

$$Q(x,t) = 0.94\alpha \frac{J_L}{t_P}(1-R)\cdot e^{\left(-2.77\left(\frac{t-\frac{t_P}{2}}{t_P}\right)^2 - \alpha x\right)} \tag{13}$$

3.1. Discretization of the TTM

To solve the differential equations given above, the finite difference method (FDM) is applied. By replacing the derivations with difference quotients, numerical solutions can be found. Using equation 8 and discretising it for the temperature in the next time- and spatial step $T_{e_k}^{n+1}$, results in the electron balance equation:

$$\begin{aligned} T_{e_k}^{n+1} = T_{e_k}^{n} + \frac{\Delta t}{C_{e_k}^{n}} \biggl(\frac{\Delta t}{2\Delta z \tau_{e_k}^{n}} \left[\left(\dot{q}_{e_{k+1}}^{n} - \dot{q}_{e_{k-1}}^{n}\right)\right. \biggr) \left(\frac{\tau_{e_k}^{n}}{\Delta t} - 1\right) - \kappa_{e_k}^{n} \frac{T_{e_{k+2}}^{n} - 2T_{e_k}^{n} + T_{e_{k-2}}^{n}}{2\Delta z} \left.\right] \\ -G(T_{e_k}^{n} - T_{i_k}^{n}) + Q_k^{n} \biggr) \end{aligned} \tag{14}$$

The discretised ion balance equation results as follows:

$$T_{i_k^{n+1}} = T_{i_k}^{n} + \frac{\Delta t \cdot G(T_{e_k}^{n} - T_{i_k}^{n})}{C_{i_k}^{n}} \tag{15}$$

3.2. Simulation of the temperature

As a time step width, 0.02 fs were chosen, the spatial step width was set to 1 nm. To determine the complex refractive index, respectively the reflectivity of the metal surface, the Drude-Lorentz oscillator model was applied [38], leading to a reflectivity of 87.6 % for aluminium [39] (in comparison to table 1, the reflectivity is over 10 % higher, this difference results from the fact, that the value in table 1 was determined with a reflectivity measurement on a surface with a roughness and the 87.6 % result from a simulation). In the following the TTM is applied to aluminium to determine the change in reflectivity and the complex refractive index during the pulse duration. The fluence of the laser source is set to $J_L = 873.01\frac{J}{m^2}$. Heat radiation at the substrate surface is given by Planck's law [40]:

$$I_{HR} = \epsilon k_B T^4 \tag{16}$$

with the intensity of the heat radiation I_{HR}, the emissivity ϵ and the Boltzmann constant k_B. This causes electron temperatures of 15,000 K (see Fig. 5(a)), leading to an ion temperature of 774 K. Consequently, the change in the refractive index results in 5 % and that in the reflectivity 0.7 % (see Fig. 5(b)). The ion temperature of 774 K is smaller than the melting point at 933 K, so no material will be melt. Considering Wien's displacement law, electron temperatures of

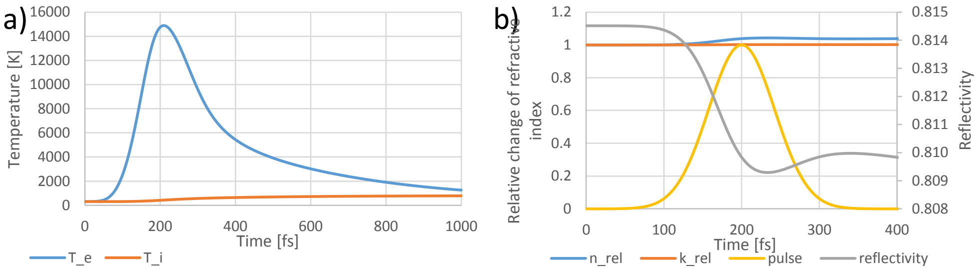

Fig. 5. (a) Electron- and ion temperature in dependence on the time, (b) Relative change of the refractive index and the extinction index in dependence on the time, the laser pulse and the reflectivity.

7430 K cause the material to emit radiation at 390 nm, which is the exposing wavelength in TPP. Thus, during the decomposition of the imbalance between electrons and ions, polymerization processes on the substrate could be influenced. With increasing temperatures, the spectrum is shifted to smaller wavelengths, so the radiation takes influence until the electron temperature has fallen beyond 7430 K. For all calculations, a wavelength of 780 nm, a pulse duration of 100 fs and a repetition rate of 80 MHz as well as an initial temperature of 298K was used.

With regard to the experimental part, where the substrate temperature is changed during TPP, the reflectivity was calculated with the TTM for different initial temperatures. These temperatures were chosen to be between 278 K and 1240 K. On the one hand, the temperature variation in the experimental part was performed between 278 K and 358 K (compare Fig. 10), on the other hand, the maximum temperatures calculated on steel with the HCE for 10 mW to 50 mW was between 487 K and 1240 K (compare 3). The reflectivity due to this temperature variation decreased by 0.025, see Fig. 6(a).

To also consider the influence of the laser beam interacting with the metal surface, when the focus is in a distance of 20 μm from the substrate surface (as it is the case for the upper planes of the cubes written in chapter 4), the laser fluence on the metal surface was calculated in dependence on the focus distance from the surface, see Fig. 6(b). At a distance of 20 μm, the fluence has fallen by a factor of 10^4 in comparison to the the situation, when the laser is focused on the surface. Comparing the electron temperatures, a decrease from 15,000 K to 340 K occured. The ion temperature fell from 772 K to 300.9 K, meaning that the temperature change due to interaction of laser and metal does not affect polymerization at higher distances from the substrate.

4. Experimental

TPP was performed with a Photonic Professional device in combination with a galvoscanner-based upgrade for higher writing speeds, both from Nanoscribe GmbH. The instrument was used in the so called Dip-in Laser Lithography (DiLL) mode, where the beam of a pulsed fibre laser with a wavelength of 780 nm is guided through a 63x microscope objective with a numerical aperture of 1.3. The objective directly immerses into the photosensitive polymer and focuses the laser on the bottom side of the substrate. Due to the spatial and temporal bundling of the laser power, the energy density within a volumetric pixel (voxel) in the focus is high enough to activate the photoinitiator in the polymer and thus start the polymerization reaction. By moving the laser beam through the polymer in lateral direction and the substrate in axial direction, arbitrary, up to three dimensional structures can be realized.

As photosensitive polymers, IP-Dip from Nanoscribe GmbH and OrmoComp from microresist technology GmbH (MRT) were used. The corresponding developers and adhesion promoters

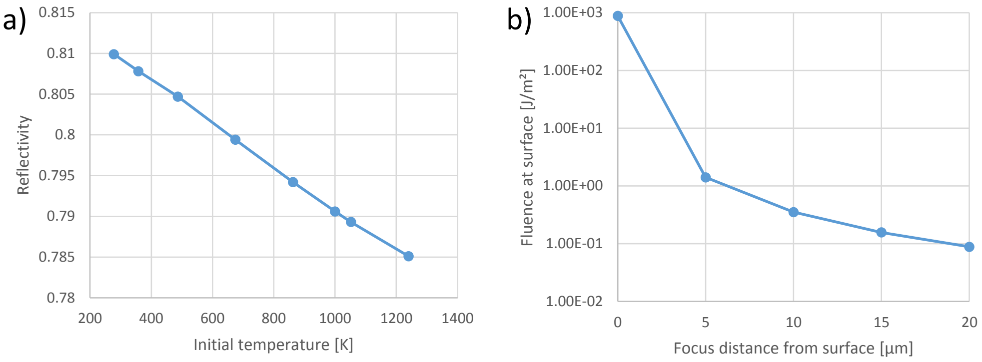

Fig. 6. (a) Change of reflectivity in dependence on the initial temperature between 278 K and 1240 K. Within this range, the real part of the refractive index increased linearly from 2.636 to 3.129, (b) Laser fluence at the metal surface in dependence on the focus distance from the surface.

were TI Prime from MicroChemicals GmbH and mrDWL from MRT for IP-Dip and OrmoPrime and OrmoDev for OrmoComp, both from MRT. Steel platelets of type 1.4310 with a size of 50 x 50 x 0.6 mm^3 served as substrates.

The aim of the experimental part is to examine the influence of temperature on the TPP process. Cubes were written on steel substrates by varying the exposure dose via the laser power. The same experiment was performed for different substrate temperatures, while the substrate was tempered as follows: For cooling and heating, the Peltier element PF 127-14-25-S from Telemeter Electronic GmbH in combination with the power supply unit EA-PS 3150-04-B from EA Elektro-Automatik GmbH & Co. KG was used. Heat was dissipated from the Peltier element during cooling by a heat sink (LA ICK 17 x 17 F 12) with an integrated cooling fan. A thermal paste enhanced the thermal conductivity between the Peltier element and the steel substrate. To measure the temperature during experiments, a platinum resistance thermometer (PT100) was used in combination with a digital multimeter. The reflectivity was measured over a range of 250 to 1300 nm and here the values for 780 nm at 298 K are used.

Fig. 7 depicts the set up for tempering the substrate during TPP. At the bottom side of the substrate, where the structures are written, the PT100 element is fixed beside the polymer area to control the surface temperature of the substrate. Temperature was set by the direct current value of the power supply. Scanning electron microscope (SEM) measurements of the structures were taken with a Zeiss Neon 40 EsB device from ZEISS AG.

4.1. Heating of metal substrates during TPP

To examine the influence of temperature on the TPP process, structures were written on steel substrates. Experiments with TPP were repeated for different temperatures from 5°C to 80°C .

As test structures, cubes were defined (see table 2), where the exposure dose was varied by the laser power (see table 2). The goal of this parameter variation was to write also under- and overexposed structures to observe how the usable power dynamic range changes with the temperature. In addition, different heights were realized, to find out, if certain effects during tempering occur at specific axial distances from the substrate. Fig. 8 shows the complete structure at room temperature.

The substrates were cooled down, respectively heated from 5°C to 80°C, while the room temperature was measured to be 21,3°C. Tests were carried out for the two photosensitive polymers IP-Dip and OrmoComp. In addition, the structuring beam was focussed before each

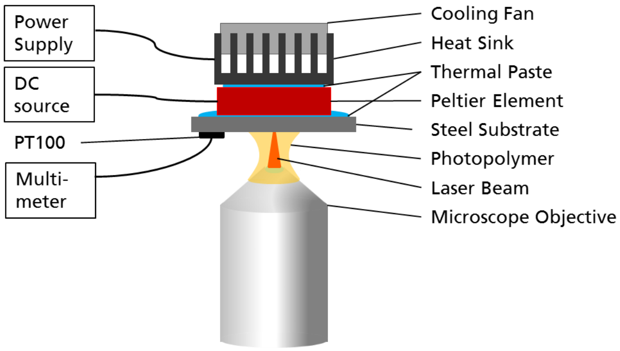

Fig. 7. Set up for temperature variation during TPP.

Table 2. Parameters of the teststcubes for temperature variation.

Edge length	Line distance [µm]	Laser power [mW]	Writing Speed $[\frac{\mu m}{s}]$	Number of planes	Height [μm]
20 µm	0.2	8, 12, 16, 20, 24	5000	25, 50, 75, 100	5, 10, 15, 20

row, to exclude missing structures due to poor adhesion. Fig. 9 shows the classification of the different polymerization grades. Phase 1 and 2 correspond to underexposure, while in phase 2, the shape of the geometry is already visible in contrary to phase 1, where only a small part of the geometry is polymerized. In phase 3, the laser power value is ideal, so a structure with high shape accuracy is realized. Overexposure is defined by phase 4, were the shape accuracy is reduced by too much energy input and blistering occurs.

4.2. Results for IP-Dip

Fig. 10 shows the cubes written in IP-Dip for temperatures from 5°C to 80°C. It becomes clear, that the energy input is reduced with increasing temperature. While for 5°C to 20°C, phase 4, corresponding to overexposure, dominates, no overexposure is observed from 30°C to 80°C. Phase 3 (ideal laser power) is present up to 40°C and from 50°C to 80°C only underexposure occurs.The respective phases 2 and 3 become smaller with higher temperatures, so from 60°C to 80°C all structures are underexposed (phase 1).

The insets in Fig. 10(c) and (g) illustrate, how the surface quality changes with increasing temperature. For 20 °C the surface is even and the single writing lines are partly visible. At 60°C, the surface texture has become rough and grainy.

Fig. 10(a) to (c) demonstrate, that the energy input is higher in the lower planes of a cube, since blistering is more present here. This effect can be explained by the back reflection of a spheric wave at the metal surface. Due to divergence, the energy and thus the laser power is damped with increasing axial distance from the surface, so less energy is present in the upper planes of a cube. Fig. 10(f), right column, also emphasizes this assumption, because the cube with the smallest number of planes has a good shape accuracy and the cube with the highest number of planes is underexposed. This is the reason, why in Fig. 10(a) to (c) the cubes in the two right coloumns are marked as overexposed, although most of them look like they were exposed with the correct dose. Fig. 6(b) and the corresponding discussion about the influence of the laser fluence on the temperature confirm this observation: A higher distance of the focus from the

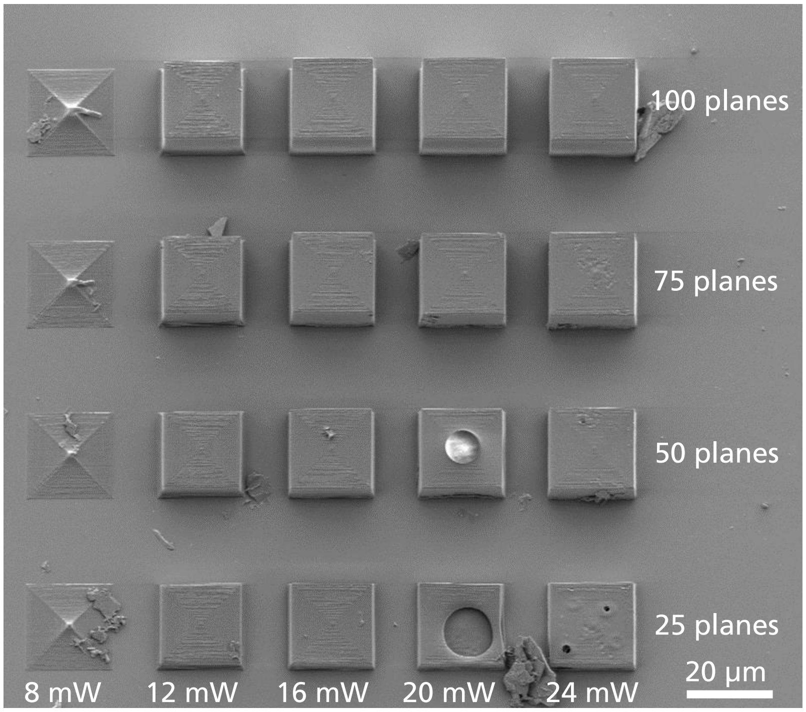

Fig. 8. Test cubes for temperature variation at room temperature in IP-Dip, each written with 5000 $\mu m/s$. The number of planes is reduced from up to down.

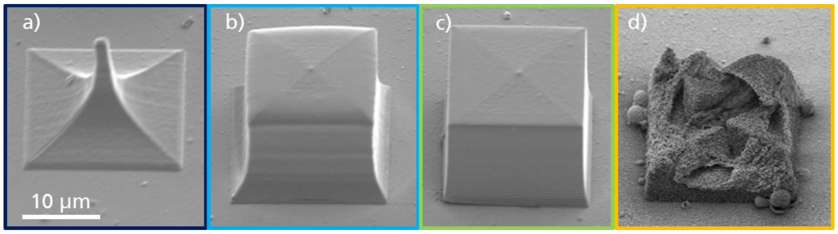

Fig. 9. Definition of the different exposure phases by the example of the cube.

substrate surface causes the laser fluence on the surface to decrease exponentially, which makes the metals temperature not to change anymore due to the radiation.

4.3. Results for OrmoComp

For OrmoComp, the maximum energy input was reached at 30°C, since it is the only setting, where overexposure occured. With increasing temperatures, less structures are realized at ideal laser power values and underexposure dominates. Regarding structures with different heights, overexposure in the lower planes in comparison to the upper planes cannot be observed. Fig. 11(a) middle column, (f) middle column and (i) second column from right show, that with additional planes, the footprint of a cube becomes larger. It can be assumed that laser power, which did not lead to polymerization is saved in the unexposed polymer, so polymerization occurs faster, when the area is exposed a second time (compare also [7]). Related to IP-Dip, the shrinking in the upper planes is more present.

To find out, at which laser powers blistering occurs at higher temperatures, the experiments for

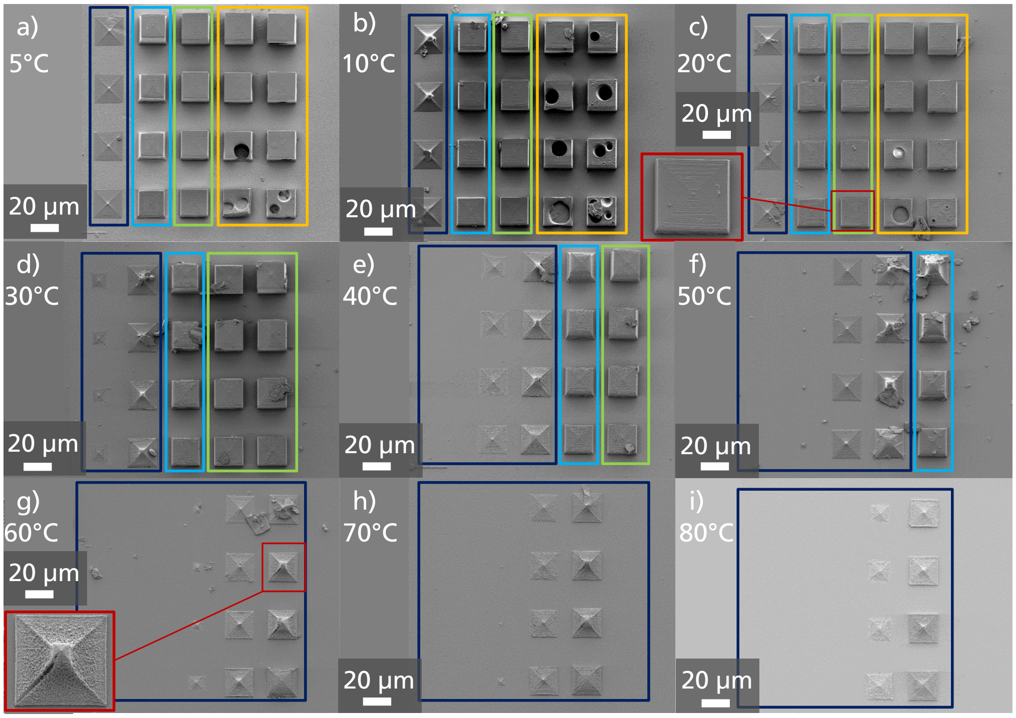

Fig. 10. Cubes in IP-Dip with constant writing speed and decreasing number of planes (from up to down, see Fig. 8) for different temperatures. From left to right, the laser power increases in each picture corresponding to Fig. 8.

50°C and 80°C were repeated with a larger laser power range from 10 mW to 65 mW, compare Fig. 12. Results showed, that blistering occured at 35 mW for 50°C and at 55 mW at 80°C. For 80°C, blistering occured that strong from 60 mW, that no polymerization process was possible anymore, since the substrate surface was not visible for the autofocus.

At 10°C and 30°C, extremely strong blistering occurred, resulting in a Turing pattern over an area, much larger than the structured area (see Fig. 11(b), (d) and Fig. 13). This effect was only observed for OrmoComp, giving the hint to an underlying reaction-diffusion-problem [41]. As introduced by Nitin Uppal et al. [42] (and applied to Ormoceres in [43]), polymerization by TPP can be described by five coupled differential equations (DEQ), giving the change of the temperature and the concentrations of the monomer, the photoinitiator, the radical and the inhibitor. Beside the equation for the temperature, all other DEQ contain a term for diffusion. In addition, the five DEQ are coupled to show, that the regarded quantities influence each other. The diffusion terms are caused by concentration gradients of the regarded quantities. During TPP, polymerization is induced very locally, so large concentration gradients occur and diffusion becomes very important. Thus, we can say, that the reactions are diffusion controlled and TPP is based on a diffusion-controlled system.

Turing patterns are also known as diffusion-driven instabilities. In literature, the stability of reaction-diffusion systems is often described by two coupled, partial differential equations, each containing diffusion terms. The solution is given by an exponential function, according to plane waves, described by wavenumbers. While for ordinary differential equations, it is interesting to find the range, where the stationary state is stable, for the reaction-diffusion-equation, it is of high interest, in which parameter range the spatially homogenous state is not stable. When doing these stability analysis mathematically, one has to find the relation between the Eigenvalue of the

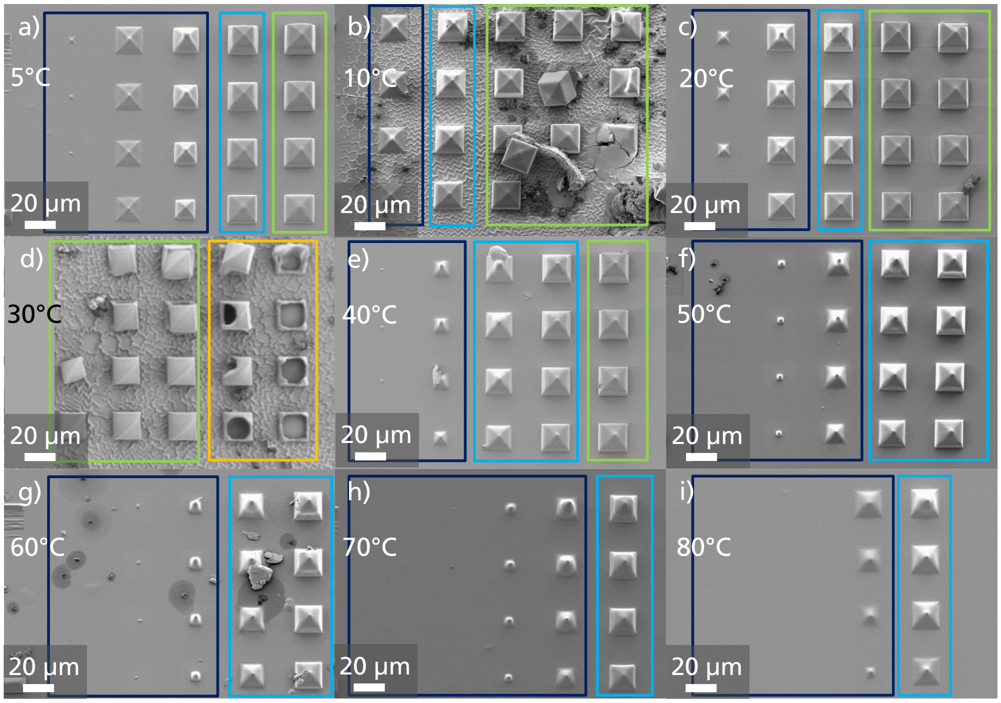

Fig. 11. Cubes in OrmoComp with constant writing speed and decreasing number of planes (from up to down) for different temperatures. From left to right, the laser power increases from 10 mW to 30 mW in 5 mW steps from left to right.

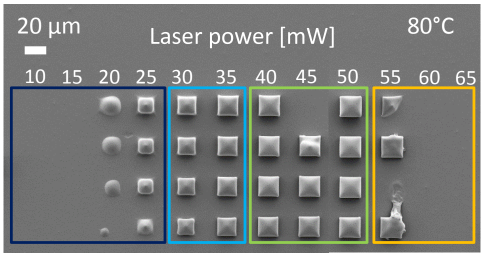

Fig. 12. SEM picture of cubes written at 80°C from 10 mW to 65 mW with a writing speed of 5000 $\mu m/s$.

matrix resulting from the differential equations and the wavenumber describing the exponential solution, leading to a curve that describes the square of the wavenumber in dependence on the Eigenvalue. This curve gives a window in which the system is unstable. Unstable means, that a perturbation in the order of the inverse of the wavenumber will be amplified by the system and causes a pattern with a corresponding wavelength (inverse of wavenumber). If the perturbation is not within the window given by the curve, it is not amplified and will not cause a Turing pattern, respectively an instability [41].

As shown in the experiments (Fig. 11), the instability occured at 10°C and 30°C, but not at 20°C. This can be explained by the fact, that there exists a specific parameter range, in which pattern formation can occur. If pattern formation occurs in this parameter range or not depends on small, statistical perturbations, respectively initial conditions. This is similar to bifurcation, where a small change of the initial condition leads to completely different results. Here, the

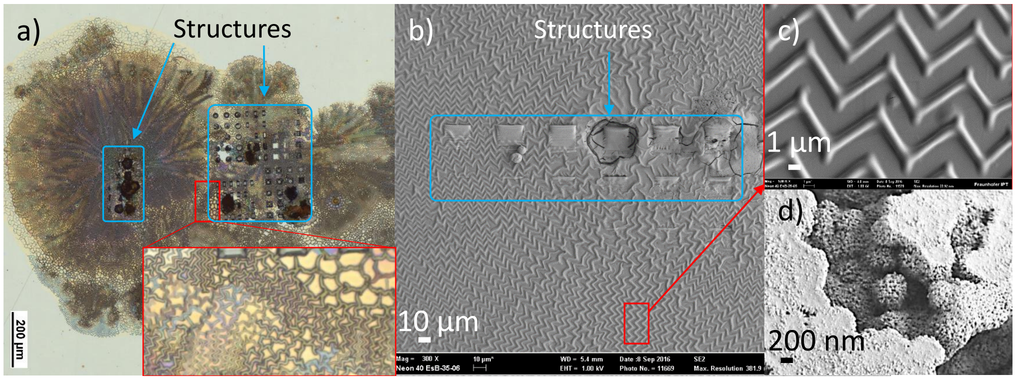

Fig. 13. Structures in OrmoComp at 30°C. Strong blistering during the writing process caused a Turing pattern (c) and small spherical polymer clusters (d).

parameter range, where a Turing pattern is possible is assumed to be between 10°C and 40°C. If the initial conditions like the distribution of the concentration of the polymer's ingredients, vary a bit, no pattern formation occurs anymore. This is a very popular effect for strong nonlinearities like reaction-diffusion systems. For higher temperatures, the necessary conditions for Turing patterns are not fulfilled anymore due to underexposure.

5. Conclusion

Within this paper the temperature in a metal substrate during TPP was calculated with the HCE as well as with the TTM. As expected, both models show a clear increase of the temperature during exposure with the laser. For the TTM, also a small amount of UV radiation is observed. To get an idea of the influence of the substrate's temperature on the polymerization process, teststructures were written in IP-Dip and OrmoComp while varying the temperature. The results show, that with increasing temperatures less polymerization occurs.

In contrast to our results, an increase of polymerization with temperature was shown in [15] and [44]. An explanation, why less polymerization occurs with higher temperatures is given by Fig. 6. The calculation with the TTM in aluminium showed, that the reflectivity decreases with higher temperatures. Considering, that above experiments were performed on steel while consulting the calculation results for steel with the HCE (see Fig. 3), it becomes clear, that steel heats up much more than aluminium for different laser powers (800 K difference for steel, 70 K for aluminium) due to the strongly reduced heat conduction (table 1). Thus, it can be assumed, that heat accumulates much more in steel in comparison to aluminium, causing a stronger decrease of the reflectivity. Additionally, an increase of the refractive index is mentioned in the caption of Fig. 6, confirming, that the material properties change significantly with the temperature. These observations lead to the conclusion, that the temperature of the metal substrate mainly influences the polymerization by changing the reflectivity and that the combination of laser power and reflectivity (in dependence on temperature) determine the optimum exposure dose. Within our experiments, the reduced reflectivity caused an underexposure of the structures.

Acknowledgement

We acknowledge Martina Vizcay Rodriguez from Fraunhofer IPT for taking the SEM pictures and Markus Lenz from the institute for semiconductor technology at RWTH Aachen University for measuring the reflectivities.

References

1. S. Maruo, O. Nakamura, and S. Kawata, “Three-dimensional microfabrication with two-photon-absorbed photopolymerization,” Opt. Lett. **22**(2), 132–134 (1997).
2. B. Jia, and M. Gu, “Two-Photon Polymerization for Three-Dimensional Photonic Devices in Polymers and Nanocomposites,” Aust. J. Chem **60**(7), 484–495 (2007).
3. F. Klein, B. Richter, T. Striebel, C. Franz, G. von Freymann, M. Wegener and M. Bastmeyer, “Two component polymer scaffolds for controlled three-dimensional cell culture,” Advanced Materials **23**(11), 1341–1345 (2011).
4. M. Roehrig, M. Thiel, M. Worgull, and H. Hoelscher, “3D Direct Laser Writing of Nano-and Microstructured Hierarchical Gecko-Mimicking Surfaces,” Small **8**(19), 3009–3015 (2012).
5. M. Baehren, H. Hartmann, G. Hein, A. Loeffler, K. Manok, J. Polzin, and U. Tober, *Photonik–Branchenreport 2013* (SPECTARIS, VDMA, ZVEI, BMBF, 2013).
6. A. Gutermuth, J. Maassen, E. Harnisch, D. Kuhlen, A. Sauer-Budge, C. Skaazik-Voogt, and K. Engelmann, “Descemet’s membrane biomimetic micro-topography differentiates human mesenchymal stem cells into corneal endothelial-like cells,” Cornea **38**, 110–119 (2018).
7. J. Fischer, and M. Wegener, “Three-dimensional optical laser lithography beyond the diffraction limit,” Laser Photonics Rev. **7**(1), 22–44 (2013).
8. E. Harnisch, and R. Schmitt, “Two-photon polymerization as a structuring technology in production: Future or fiction?” Proc. of SPIE **10115**, 101150Q1 (2017).
9. E. Harnisch, M. Russew, J. Klein, N. König, H. Crailsheim, and R. Schmitt, “Optimization of hybrid polymer materials for 2PP and fabrication of individually designed hybrid microoptical elements thereof,” Optical Materials Express **5**(2), 456–461 (2015).
10. S. Rekstyte, T. Jonavicius, and M. Malinauskas, “Direct laser writing of microstructures on optically opaque and reflective surfaces,” Optics and Lasers in Engineering **53**, 90–97 (2014).
11. S. Rekstyte, A. Zukauskas, V. Purlys, Y. Gordienko and M. Malinauskas, “Direct laser writing of 3D polymer micro/nanostructures on metallic surfaces,” Applied Surface Science **270**, 382–387 (2013).
12. S. Rekstyte, A. Zukauskas, V. Purlys, Y. Gordienko and M. Malinauskas, “Direct laser writing of 3D micro/nanostructures on opaque surfaces,” Proc. SPIE **8431**, 843123 (2012).
13. A. Zukauskas, M. Malinauskas, A. Kadys, G. Gervinskas, G. Seniutinas, S. Kandasamy, and S. Juodkazis, “Black silison: substrate for laser 3D micro/nano-polymerization,” Optics Letters **31**(9), 1307–1309 (2013).
14. C. Rheinhardt, S. Passinger, B.N. Chichkoc, C. Marquart, I.P. Radko, and S.I. Bozhevolnyi, “Laser-fabricated dielectric optical components for surface plasmon polaritons,” Optics Express **21**(6), 6901–6909 (2006).
15. E. Stankevicius, E. Daugnoraite, A. Selskis, S. Juodkazis, and G. Raciukaitis, “Photo-polymerization differences by using nanosecond and picosecond laser pulses,” Optics Express **25**(5), 4819–4813 (2017).
16. T. Bückmann et al., “Tailored 3D mechanical metamaterials made by dip-in direct-laser-writing optical lithography,” Optical Materials Express **24**(20), 2710–2714 (2012).
17. R. Poprawe, *Lasertechnik fuer die Fertigung* (Springer-Verlag Berlin Heidelberg, 2005).
18. A. Date , *Introduction to Computational Fluid Dynamics* (Cambridge University Press, 2005).
19. H.K. Versteeg, and W. Malalasekera, *An Introduction to Computational Fluid Dynamics – The Finite Volume Method* (Longman Scientific & Technical, 1995).
20. C. Brecher, F. Klocke, and M. Winterschladen, “Ultraschallunterstuetztes Hartdrehen für die Fertigung von gehaerteten Praezisionsstahlbauteilen,” Wt Werkstattstechnik online **6**, 396–401 (2006).
21. J. Schneider, H. Iwanek, K.H. Zum Gahr, “Charakterisierung des Verschleißverhaltens von Formeinsatz-Werkstoffen für das Mikro-Pulverspritzgießen,” Materialwissenschaft und Werkstofftechnik **35**(10–11), 729–735 (2004).
22. Z. Zhong, M.H. Leong, and X.D. Liu, “The wear rates and performance of three mold insert materials,” Materials & Design **32**(2), 643–648 (2011).
23. T. Abeln, *Grundlagen der Verfahrenstechnik des reaktiven Laserpraezisionsabtragens von Stahl* (Herbert Utz Verlag Wissenschaft Muenchen, 2002).
24. Filmetrics, “Refractive index database,"(Filmetrics, 2014), `https://www.filmetrics.com/refractive-index-database/Stainless+Steel`.
25. Stauber Werkzeugstahl und Edelstahl, “Datenblatt 1.2083," `https://www.stauberstahl.com/werkstoffe/12083-werkstoff-datenblatt/`.
26. H.H. Binder , *Lexikon der chemischen Elemente: das Periodensystem in Fakten, Zahlen u. Daten; Mit einem Geleitw. von I. Barbur* (Stuttgart: Hirzel Verl., 1999).
27. RSP Technology, “Alloy Overview: RSP Technology RSA-905 AE Aluminium Super Alloy," `http://www.rsp-technology.com/datasheets-news.html`.
28. Deutsches Kupferinstitut Copper Alliance, “Werkstoffe: Datenblaetter," `https://www.kupferinstitut.de/de/persoenlicheberatung/downloads/downloads/werkstoffe/werkstoff-datenblaetter.html`.
29. RefractiveIndex.Info, “Refractive index database," (RefractiveIndex.INFO website, 2008-2018), `https://refractiveindex.info/?shelf=3d&book =metals&page=aluminium`.
30. RefractiveIndex.Info, “Refractive index database," (RefractiveIndex.INFO website, 2008-2018), `https://refractiveindex.info/?shelf=3d&book =metals&page=brass`.
31. S. I. Anisimov, B. L. Kapeliovich, and T. L. Perel’man, “Electron emission from metal surfaces exposed to ultrashort

laser pulses," Sov. Phys. JETP **39**(2), 375–377 (1974).

32. I. A. Abdallah, "Maxwell-Cattaneo Heat Convection and Thermal Stresses Responses of a Semi-infinite Medium due to High Speed Laser Heating," Progress in Physics **3**(12), 12–17 (2009).
33. N. W. Ashcroft, and N. D. Mermin , *Festkoerperphysik* (Oldenburg Wissenschaftsverlag GmbH, 2013).
34. P. Debye, "Zur theorie der spezifischen wärmen," Annalen der Physik **344**(14), 789–839 (1912).
35. E. Majchrzak, and Jolanta Poteralska, "Two-temperature microscale heat transfer model. Part II: Determination of lattice parameters," Scientific Research of the Institute of Mathematics and Computer Science **9**(1), 109–119 (2010).
36. J.K. Chen, W.P. Latham, and J.E. Beraun, "The role of electron–phonon coupling in ultrafast laser heating," Journal of Laser Applications **17**(1), 63–68 (2005).
37. L. Jiang, and H.-L. Tsai, "Improved Two-Temperature Model and Its Application in Ultrashort Laser Heating of Metal Films," Journal of Heat Transfer **127**(10), 1167–1173 (2005).
38. Mathworks, "Drude-Lorentz and Debye-Lorentz models for the dielectric constant of metals and water," (MathWorks website, 1994-2018), `http://de.mathworks.com/matlabcentral/fileexchange/18040-drude-lorentz-and-debye-lorentz-models-for-the-dielectric-constant-of-metals-and-water`.
39. A.D. Rakic et al., "Optical properties of metallic films for vertical-cavity optoelectronic devices," Applied Optics **37**(22), 5271–5283 (1998).
40. P.A. Tipler, and G. Mosca , *Physik fuer Wissenschaftler und Ingenieure* (Springer Spektrum, 2015).
41. A.M. Turing, "The Chemical Basis of Morphogenesis," Philosophical Transactions of the Royal Society of London B: Biological Sciences **237**(641), 37–72 (1952).
42. N. Uppal, and P.S. Shiakolas, "Modeling of temperature-dependent diffusion and polymerization kinetics and their effects on two-photon polymerization dynamics," Journal of Micro/Nanolithography, MEMS, and MOEMS **7**(4), 043002 (2008).
43. T. Stichel,"Die Herstellung von Scaffolds aus funktionellen Hybridpolymeren für die regenerative Medizin mittels Zwei-Photonen-Polymerisation," PhD thesis, Julius-Maximilians-Universitaet Wuerzburg (2016).
44. I. Wang, M. Bouriau, and P.L. Baldeck, "Three-dimensional microfabrication by two-photon-initiated polymerization with a low-cost microlaser," Optics Letters **27**(15), 1348–1350 (2002).